Supporting Information

Efficient 3D charge transport in planar triazatruxene-based dumbbell-shaped molecules forming a bridged columnar phase

*Jiang Jing,[a] Benoît Heinrich,[b] Alexis Prel,[a] Emilie Steveler,[a] Tianyan Han,[a] Ibrahim Bulut,[c] Stéphane Méry,[b] Yann Leroy,[a] Nicolas Leclerc,[c] Patrick Lévêque,[a] Martin Rosenthal,[d] Dimitri A. Ivanov[e,f] and Thomas Heiser *[a]*

[a] ICube Research Institute, Université de Strasbourg, CNRS, UMR 7357, 23 rue du Loess, 67037 Strasbourg, France. *E-mail: thomas.heiser@unistra.fr*

[b] Institut de Physique et Chimie des Matériaux de Strasbourg, Université de Strasbourg, CNRS, UMR 7504, 23 rue du Loess, 67034 Strasbourg, France.

[c] Institut de Chimie et Procédés pour l'Energie, l'Environnement et la Santé Université de Strasbourg, CNRS, UMR 7515, 25 rue Becquerel, 67087 Strasbourg, France.

[d] European Synchrotron Radiation Facility (ESRF), Avenue des Martyrs 71, 38000 Grenoble, France.

[e] Institut de Sciences des Matériaux de Mulhouse, IS2M, CNRS UMR7361, 15 Jean Starcky, Mulhouse 68057, France.

[f] Faculty of Chemistry, Lomonosov Moscow State University, GSP-1, 1-3 Leninskiye Gory, 119991 Moscow, Russia.

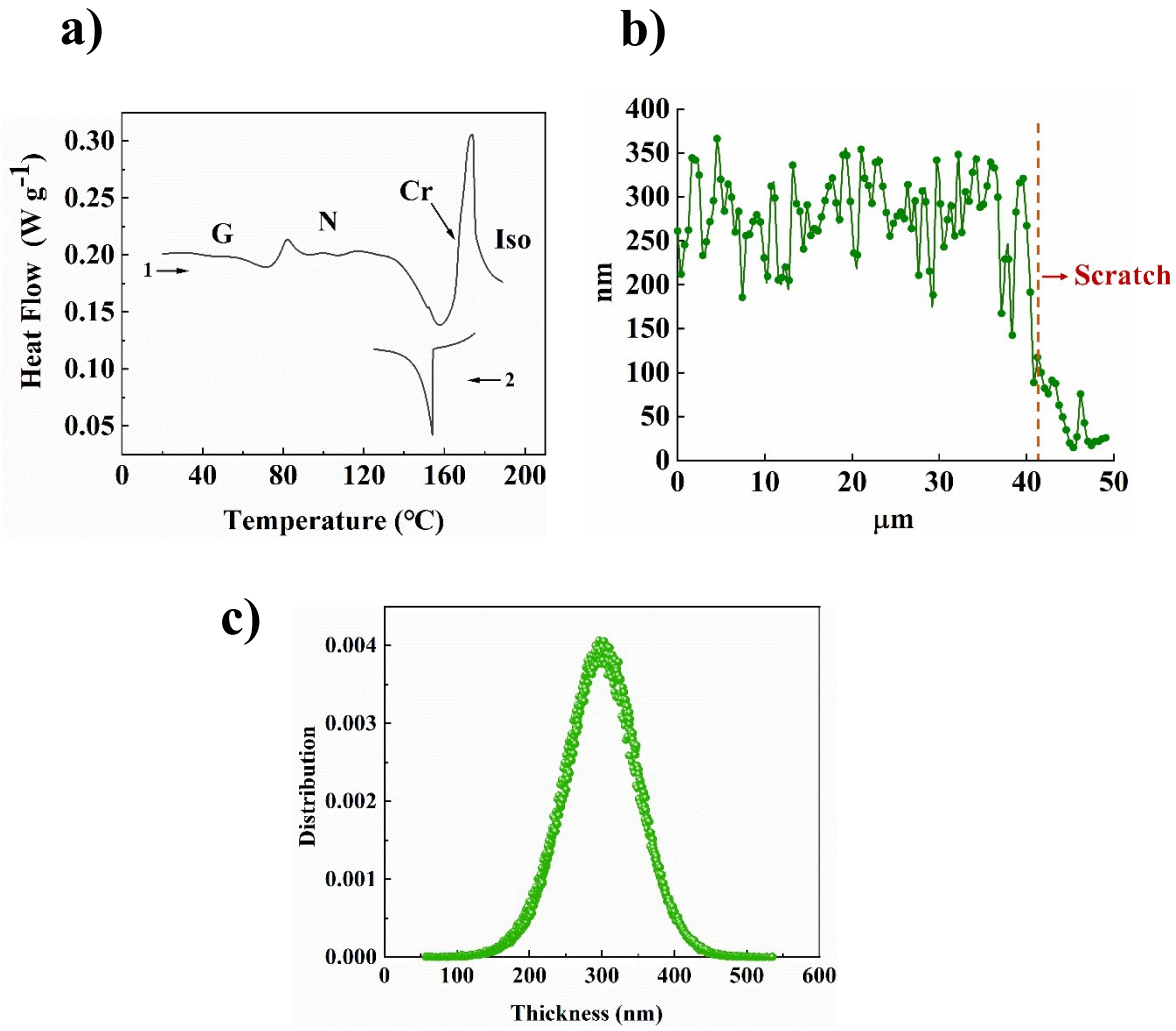

Fig. S1 (a) Differential scanning calorimetry heating scan for TPD_{C8}-TAT_{C8}. First heating run from glassy nematic state (G) to isotropic liquid phase (Iso), through fluid nematic phase (N) and crystalline phase (Cr), obtained through cold crystallization and followed by melting. 2nd cooling run from Iso to N. (b) Surface profile of a TPD_{C8}-TAT_{C8} thin film in the crystalline state as measured using atomic force microscopy (AFM) (small crystals). (c) Thickness distribution of a crystalline thin film.

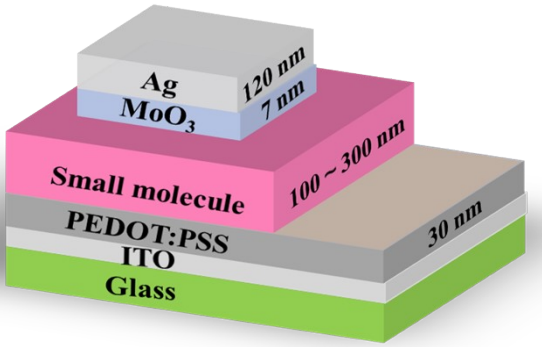

Scheme S1 Structure of a standard SCLC device.

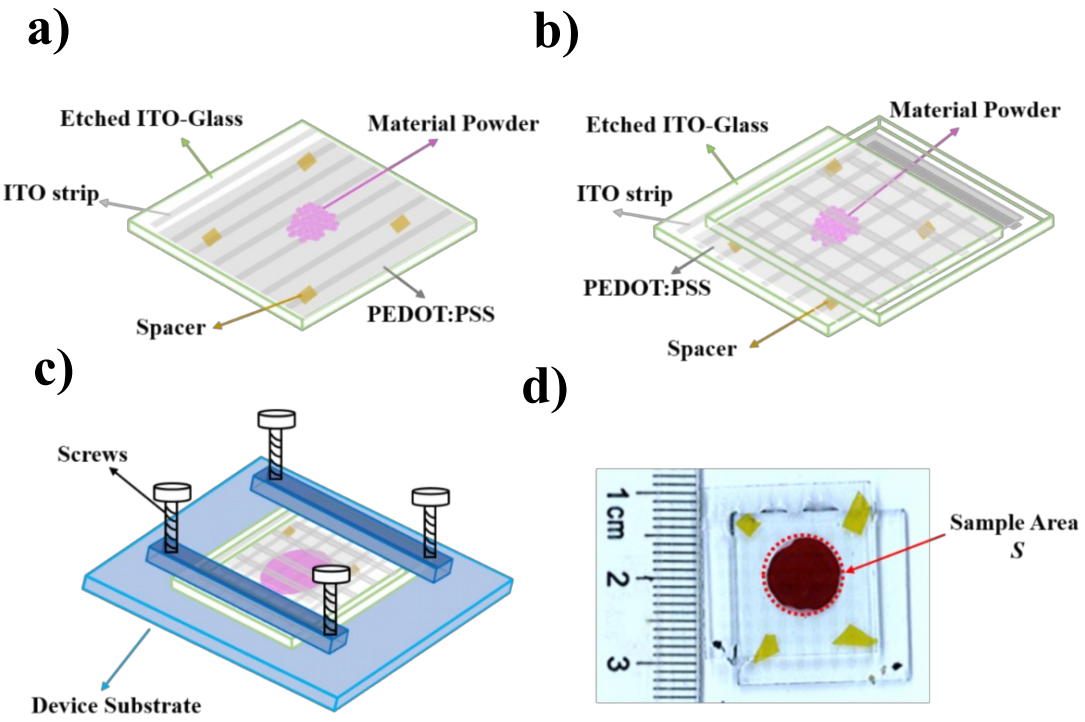

Scheme S2 Thick SCLC devices. (a) ~ (c) Fabrication procedure of thick SCLC devices. (d) Image of thick SCLC device, efficient four diodes with 1.0 mm^2 individual active area (crossing of ITO stripes).

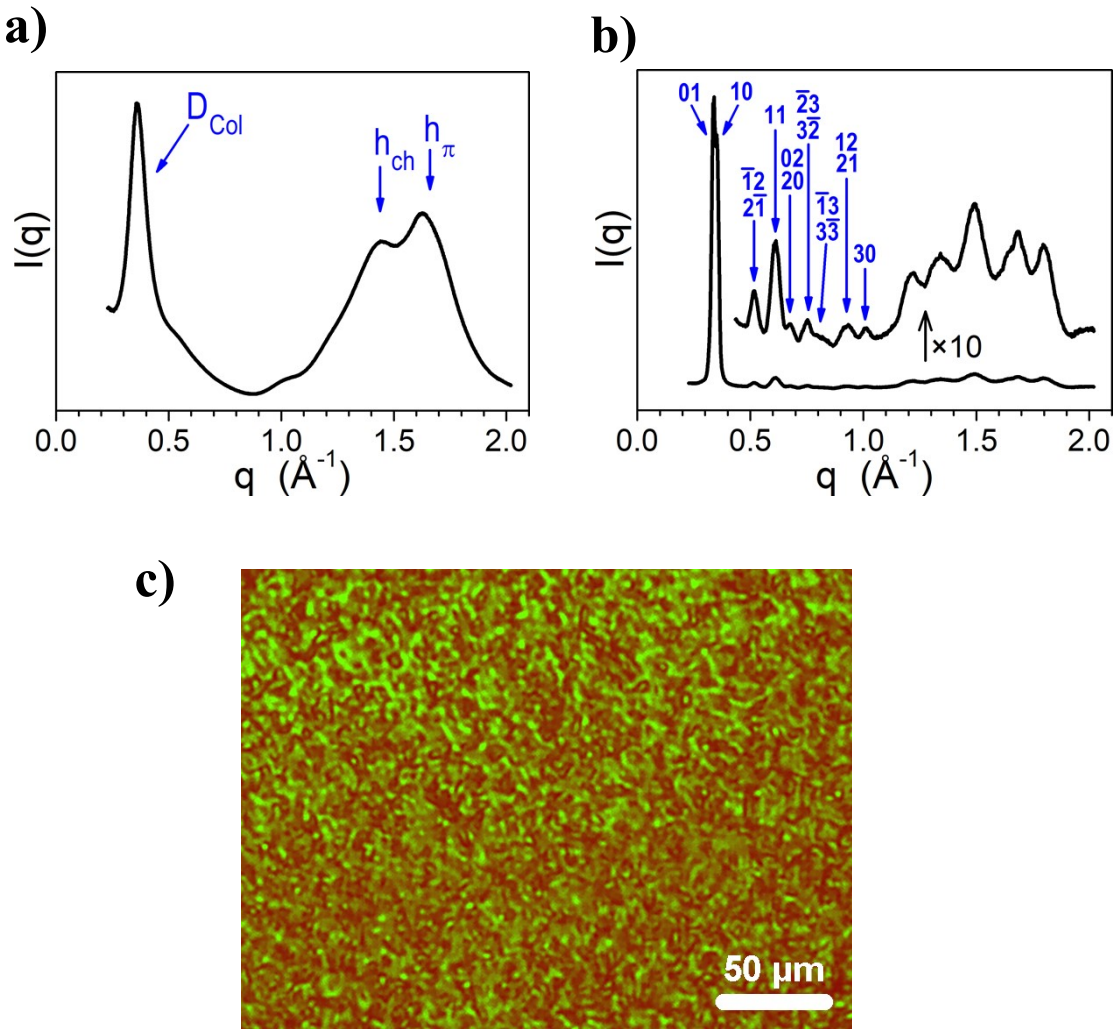

Fig. S2 Radial profiles of GIWAXS patterns: (a) Frozen mesophase (columnar-nematic state) displaying broad peaks originating from the π-stacking within columns of TAT units (h_π = 3.8 Å), packing between molten alkyl chains (h_{ch} = 4.5 Å) and lateral spacing between columns (D_{col} = 18 Å). (b) Crystal reflections of oblique sublattice in small-angle region. Reflections in wide-angle region are insufficiently resolved for the indexation of the 3D cell. (c) Polarized optical micrograph of a thick SCLC device in the nematic state prepared following the procedure described in Scheme S2 (note that the thickness was reduced with respect to SCLC devices in order to increase transparency). The bright Schlieren texture is similar to the one observed in spin-coated films and points out in-plane orientation of the nematic director.

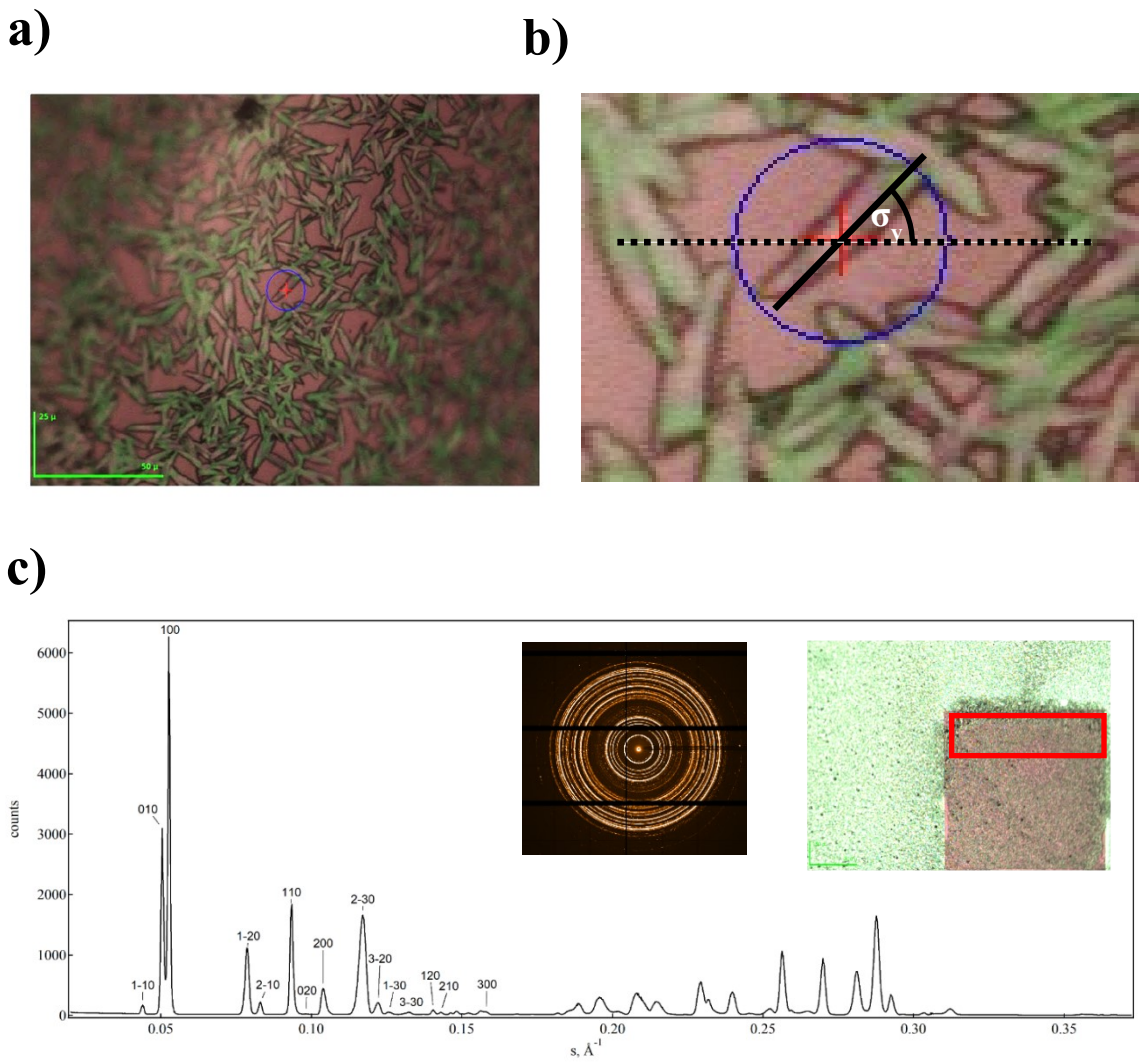

Fig. S3 (a) Layer of crystalline needles on Si_3N_4 membrane. (b) Isolated crystal on which the Microfocus X-ray diffraction measurement was done. (c) Radial profiles of Microfocus X-ray diffraction patterns. The figure insert shows the analysis of pseudo-powder data calculated for ~20'000 individual micro diffraction patterns using a maximum projection algorithm.

DEVICE MODELING

Least-square fitting $J=J_{(ohmic)}+J_{(SCLC)}$

The least-square fitting method takes advantage of the fact that the *I-V* characteristics can be approximated by equation (1) $J = q\mu_h p_o \frac{V}{L} + \frac{9}{8}\varepsilon_o \varepsilon_r \mu_h \frac{V^2}{L^3}$, as shown by Röhr and MacKenzie. [S1] This makes the procedure more robust when the SCLC region is narrow, because the entire voltage range is contributing.

Fig. S4 demonstrates the fitting approach for a standard SCLC device in the crystalline state. First, the *I-V* characteristics are fitted to equation (1), yielding an estimate for the hole mobility μ_h and the background concentration p_0 (black curve). These parameters are then fed into a 1D drift-diffusion model solved using the COMSOL Multiphysics software® [S2] (red curve). The good accordance between both curves confirms a posteriori the validity of summing the ohmic and Mott-Gurney's contributions.

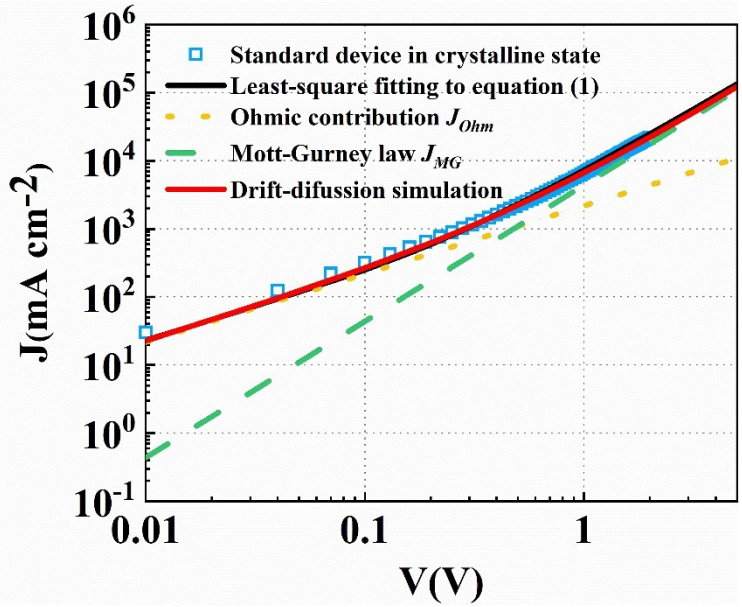

Fig. S4 Least-square fitting method for the determination of μ_h

Simulated *J-V* characteristics with rough surface profile.

In the case of standard SCLC devices, the surface roughness can lead to an overestimation of the mobility. This is because, strictly speaking, Mott-Gurney's law only applies to flat device. Due to the L^{-3} dependence of equation (1), thinner sections will contribute disproportionately to the current, such that applying Mott-Gurney with the average thickness is no longer appropriate. This is illustrated on **Fig. S5**.

Fig. S5a shows a thickness profile obtained by AFM measurement on the standard device. This profile was used to set up a 2D drift-diffusion simulation using the COMSOL Multiphysics software®, resulting in the *J-V* characteristics shown in **Fig. S5b** (black curve).

Clearly, equation (1) (green curve) using the average thickness fails to describe the SCLC regime in that case. As a result, the parameter fitting method will tend to overestimate the mobility. In the presented case for instance, a correction factor of 1.65 needs to be applied to Mott-Gurney's law to recover the *J-V* characteristics (shown as a red dotted line on **Fig.S5**). As a result, μ_h would be overestimated by 65%.

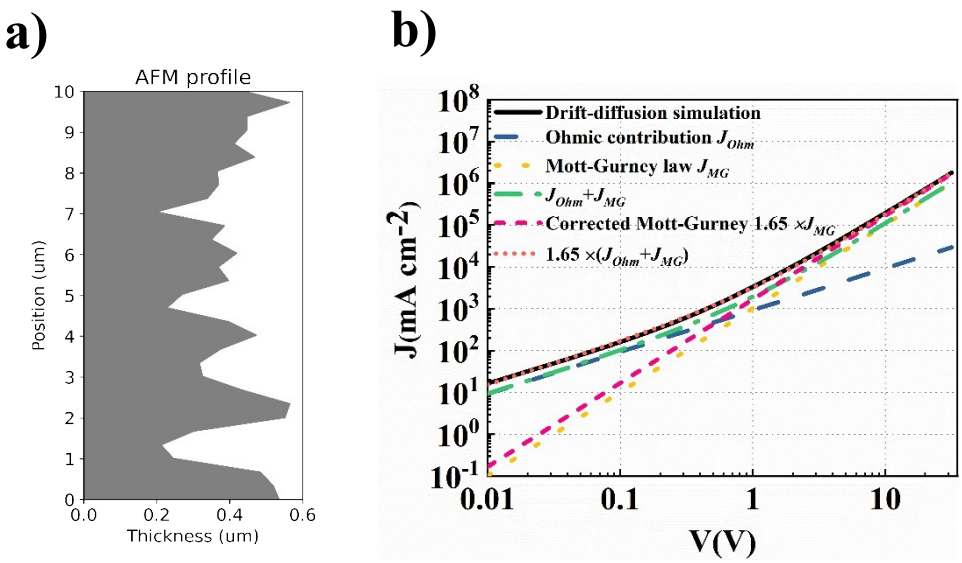

Fig. S5 Consequence of surface roughness on Mott-Gurney's law applicability. (a) AFM profile across a 10 µm wide representative region. (b) Simulated *J-V* characteristics resulting from the rough profile.

References

[S1] J. A. Röhr, R. C. I. MacKenzie, *J. Appl. Phys.* 2020, **128**, 165701.

[S2] COMSOL Multiphysics® v. 5.5. www.comsol.com. COMSOL AB, Stockholm, Sweden.

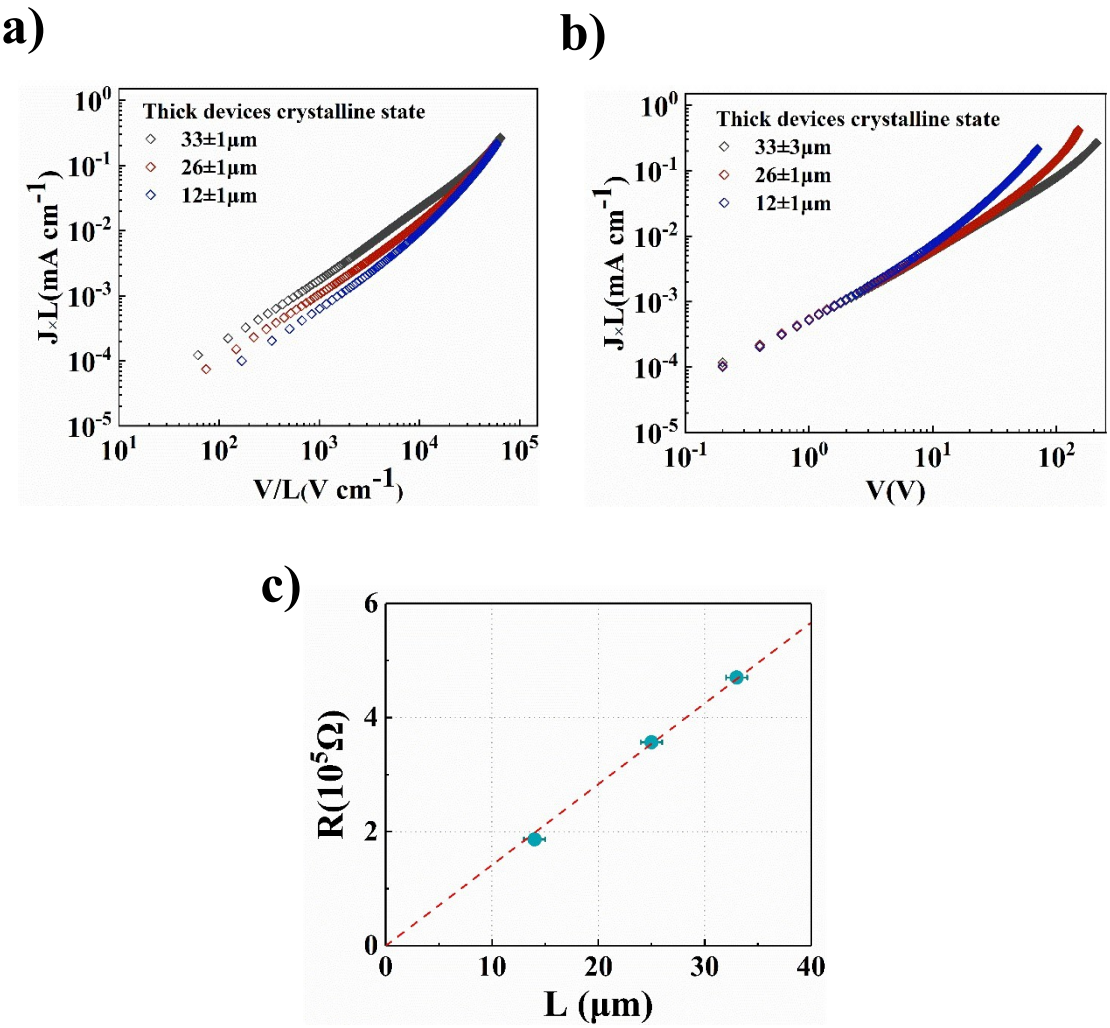

Fig. S6 *J-V* characteristics of thick SCLC devices at 296 K with different film thicknesses. (a) $J \times L$ as a function of V/L: the curves overlap in the SCLC part, as predicted by equation 1 (Mott-Gurney term). (b) $J \times L$ as a function of V: the curves overlap in the ohmic part, as predicted by equation 1 in case of a constant background carrier concentration. (c) Ohmic resistances estimated from the ohmic part of the *J(V)* curves of thick crystalline devices as a function of the layer thickness.

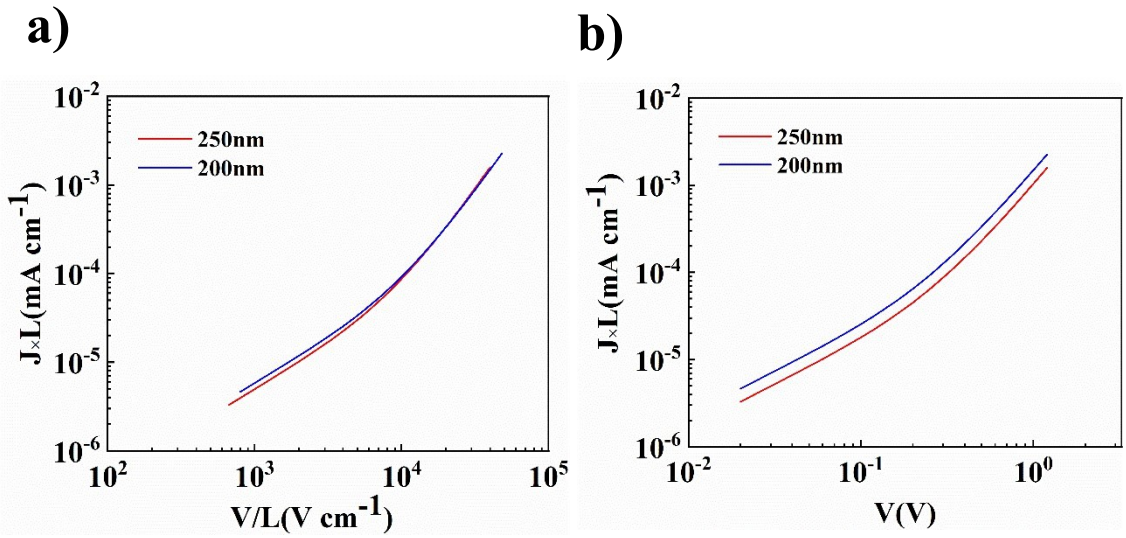

Fig. S7 *J-V* characteristics of standard SCLC devices in the columnar-nematic state. (a) $J \times L$ as function of V/L: the curves overlap in the SCLC part, as predicted by equation 1. (b) $J \times L$ as a function of V: the curves do not overlap in the ohmic part, suggesting that the average background carrier concentration depends on the applied voltage.

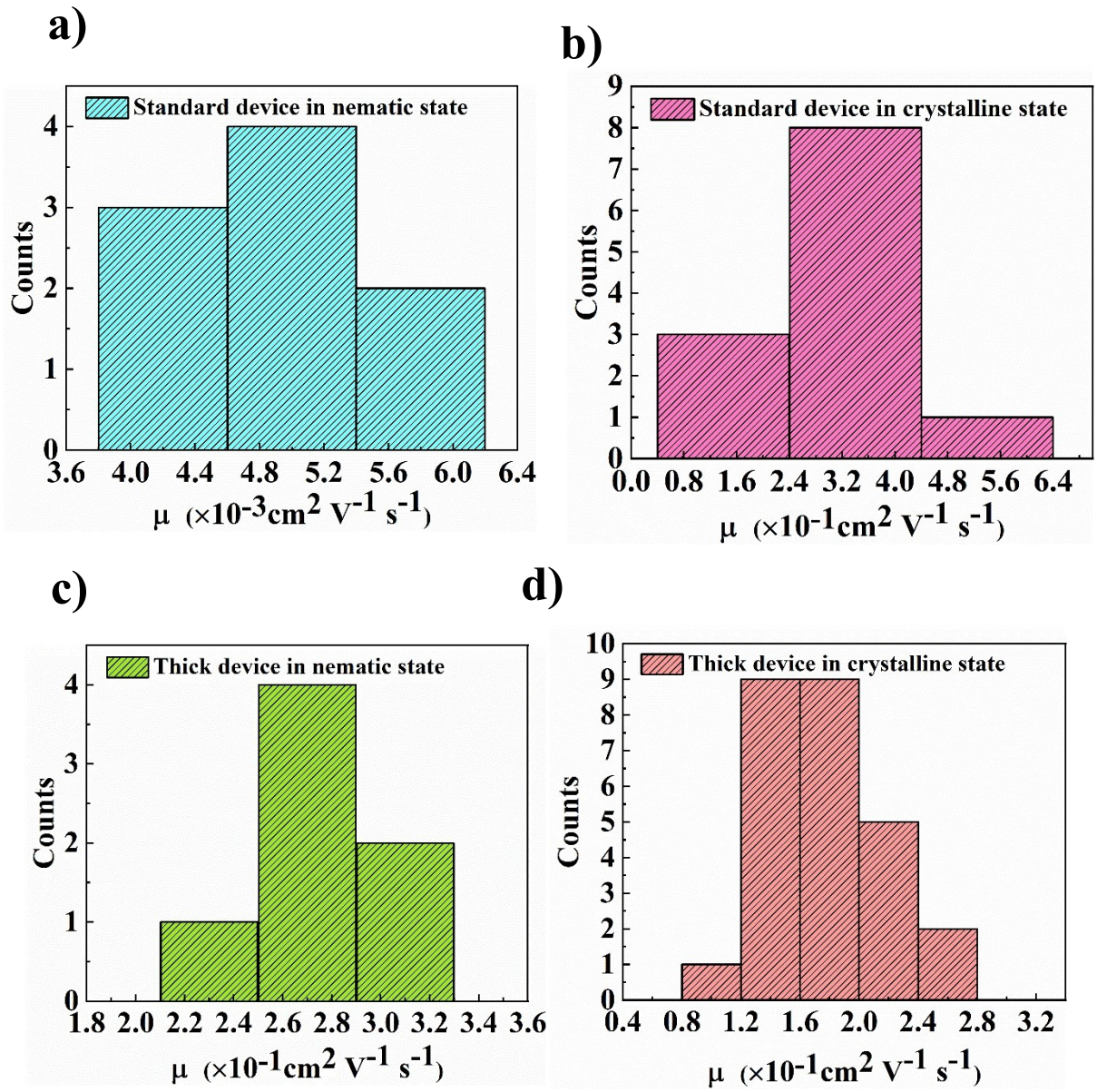

Fig. S8 Histograms of SCLC measurements. (a) Standard SCLC devices in columnar-nematic state, thickness is 250±10nm. (b) Standard SCLC devices in crystalline state, thickness is 300±60 nm. (c) Thick SCLC devices in columnar-nematic state, thickness is 21±1μm. (d) Thick SCLC devices in crystalline state, three different thickness is 33±1μm, 26±1μm, 12±1μm, respectively. The width of the columns represents the error margin on film thickness and mobility measurements.

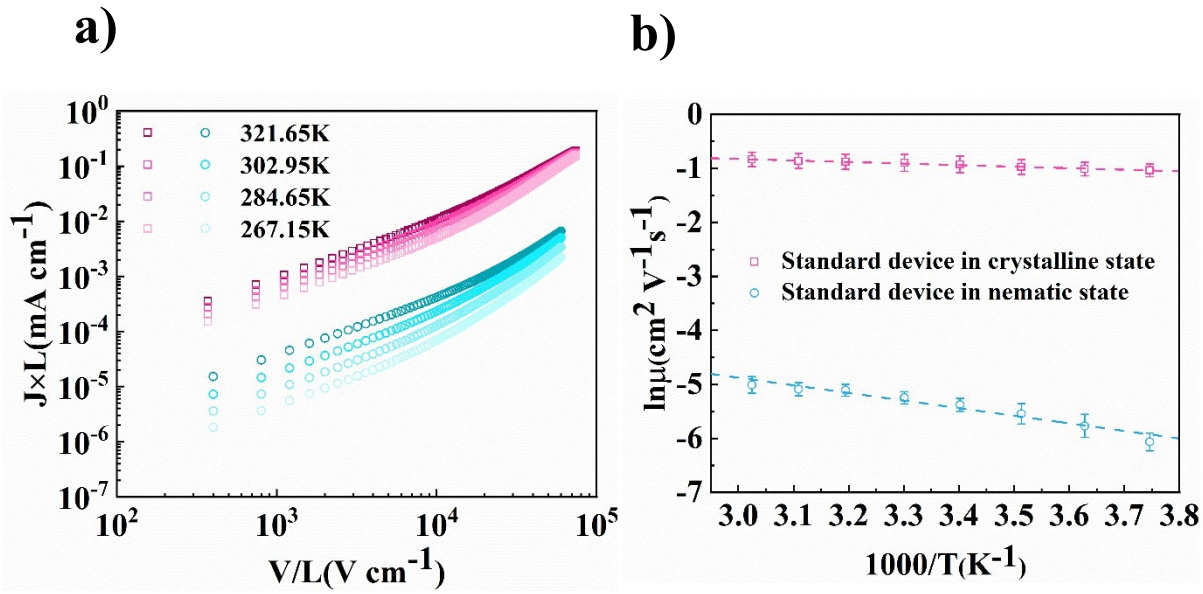

Fig. S9 (a) *J-V* characteristics as a function of temperature on standard SCLC devices, in the crystalline state (open red squares) and columnar-nematic state (open blue dots). (b) Arrhenius plots of the hole mobility. Error bars estimated from measurements on four individual diodes.

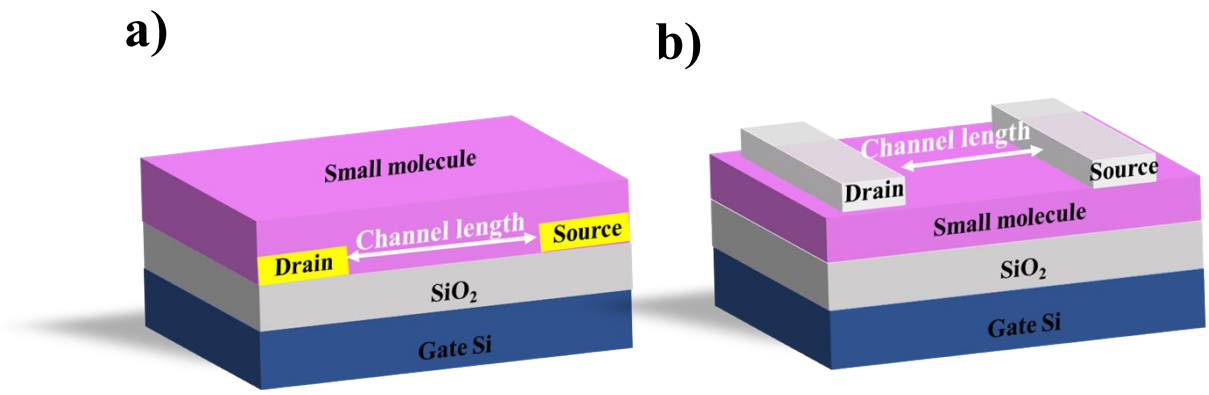

Scheme S3. OFET device structures. (a) Bottom-contact-bottom-gate transistors, with ITO/Au bilayers used as drain and source electrode. (b) Top-contact-bottom-gate transistors, with MoO_3/Ag layers used as drain and source electrode.

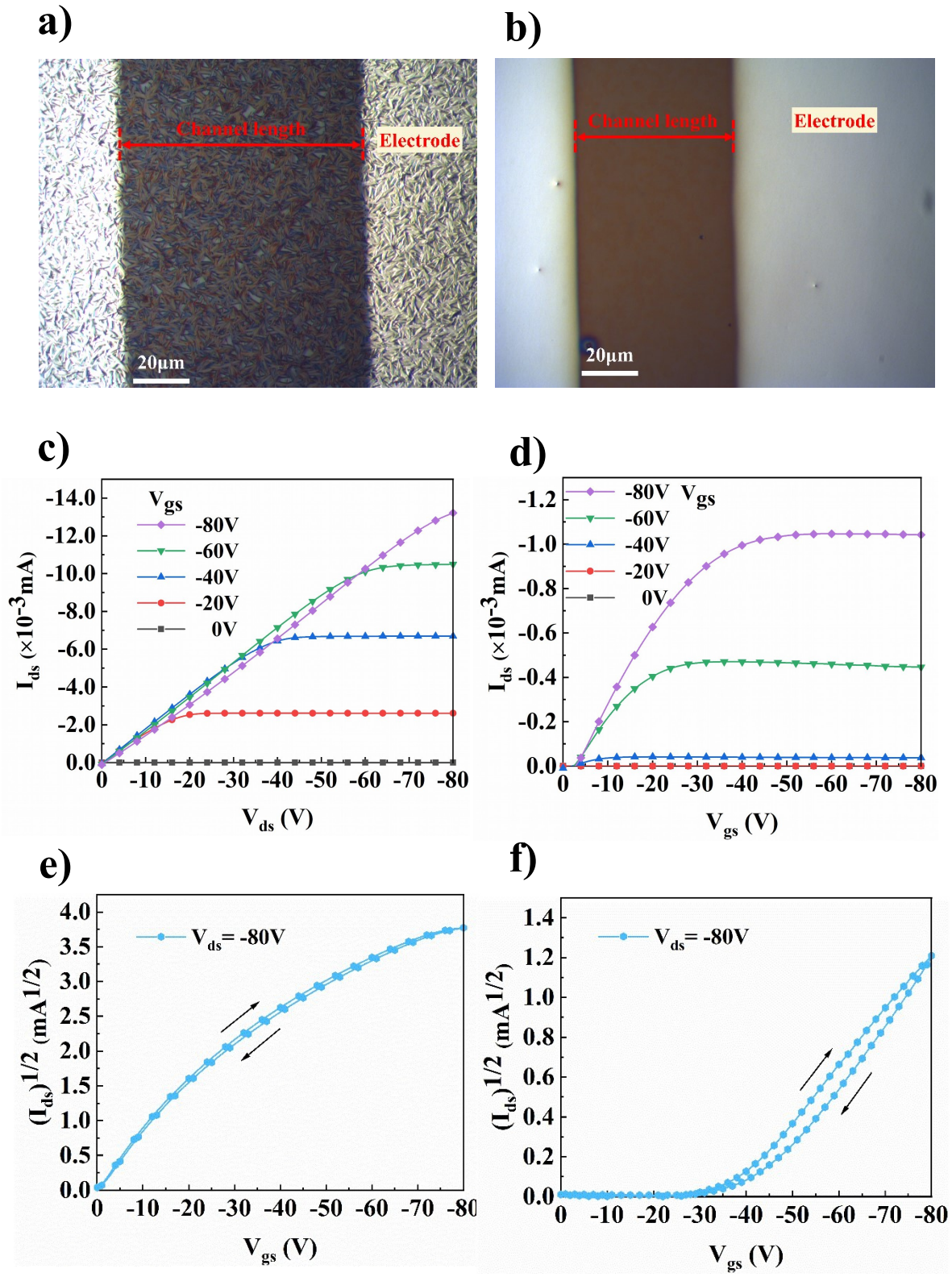

Fig. S10 Top-contact-bottom-gate transistors device. Optical micrographs of a transistor in (a) the crystalline state and (b) the columnar-nematic state. Output characteristics for (c) the

crystalline state and (d) the columnar-nematic state. Transfer characteristics in the saturation regime for (e) the crystalline state and (f) the columnar-nematic state.

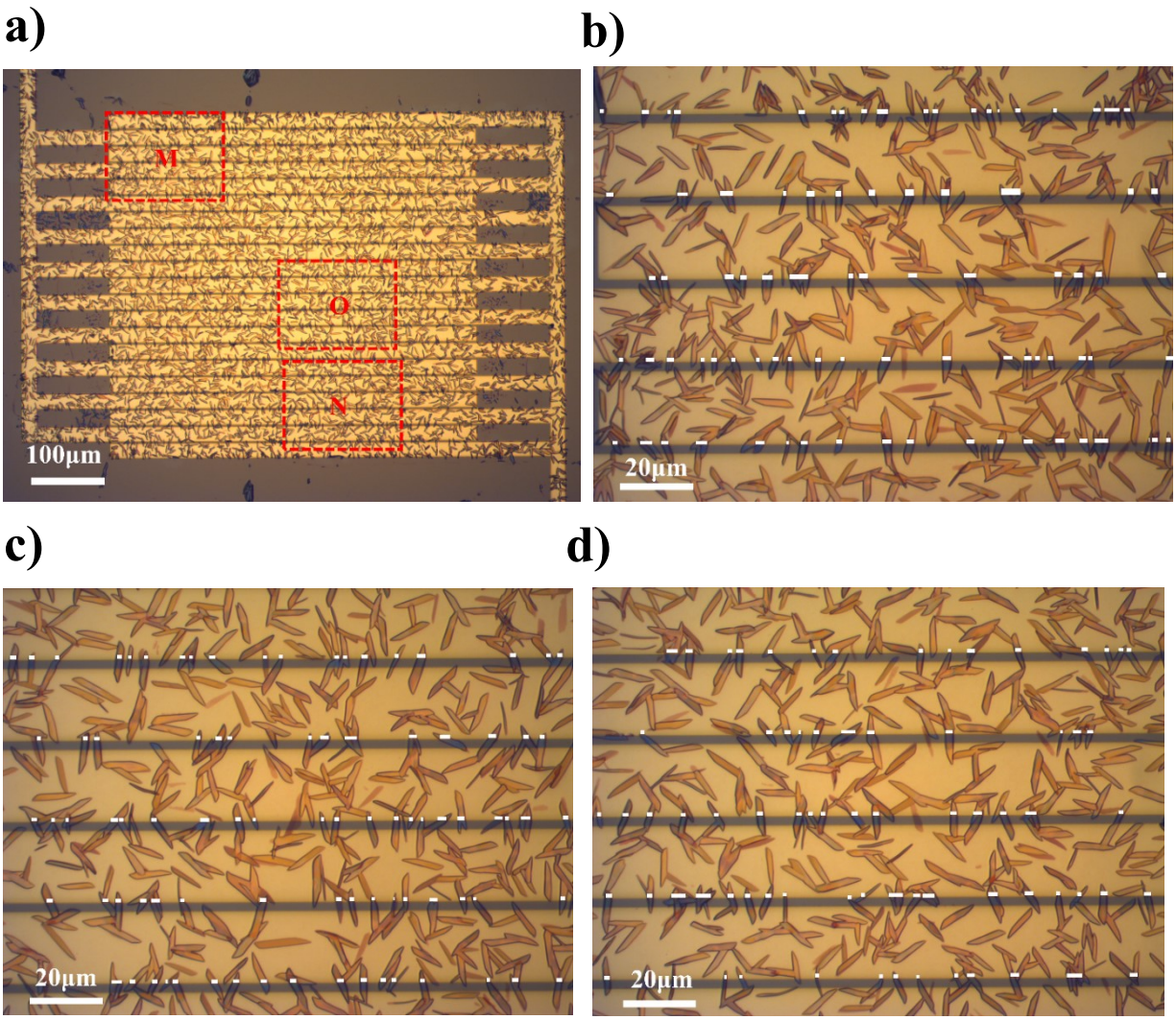

Fig. S11 Optical micrographs of bottom-contact-bottom-gate transistor with a 2.5 µm channel length and 1.0 cm channel width. (a) Full device. (b), (c) and (d) zoom ×5 of three regions used to estimate the fraction of channel width covered by the crystalline needles. The corresponding effective channel width is 0.17±0.02 cm.

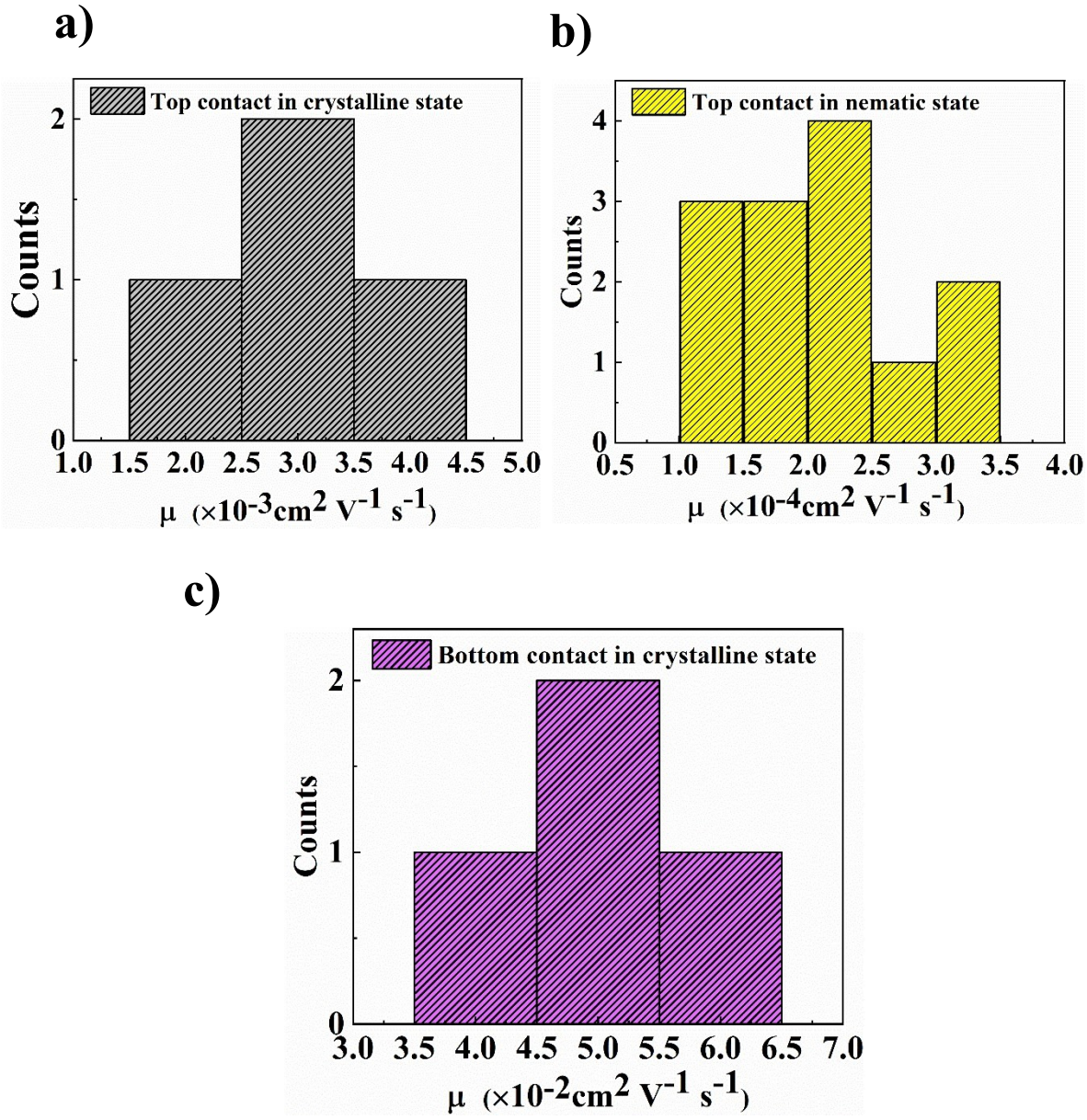

Fig. S12 Histograms for field-effect mobility data. (a) Top-contact-bottom-gate transistors in the crystalline state (average crystal size ≈ 2.5 μm, channel length = 90 μm, channel width= 3.646 cm). (b) Top-contact-bottom-gate transistors in the nematic state (channel length= 60 μm, channel width = 2.917 cm). (c) Bottom-contact-bottom-gate transistors in the crystalline state (average crystal size ≈ 10 μm, channel length= 2.5 μm, channel width= 0.17±0.02 cm as estimated from Figure S11). The width of the columns represents the error margin on the channel width estimation and hole mobility extraction.

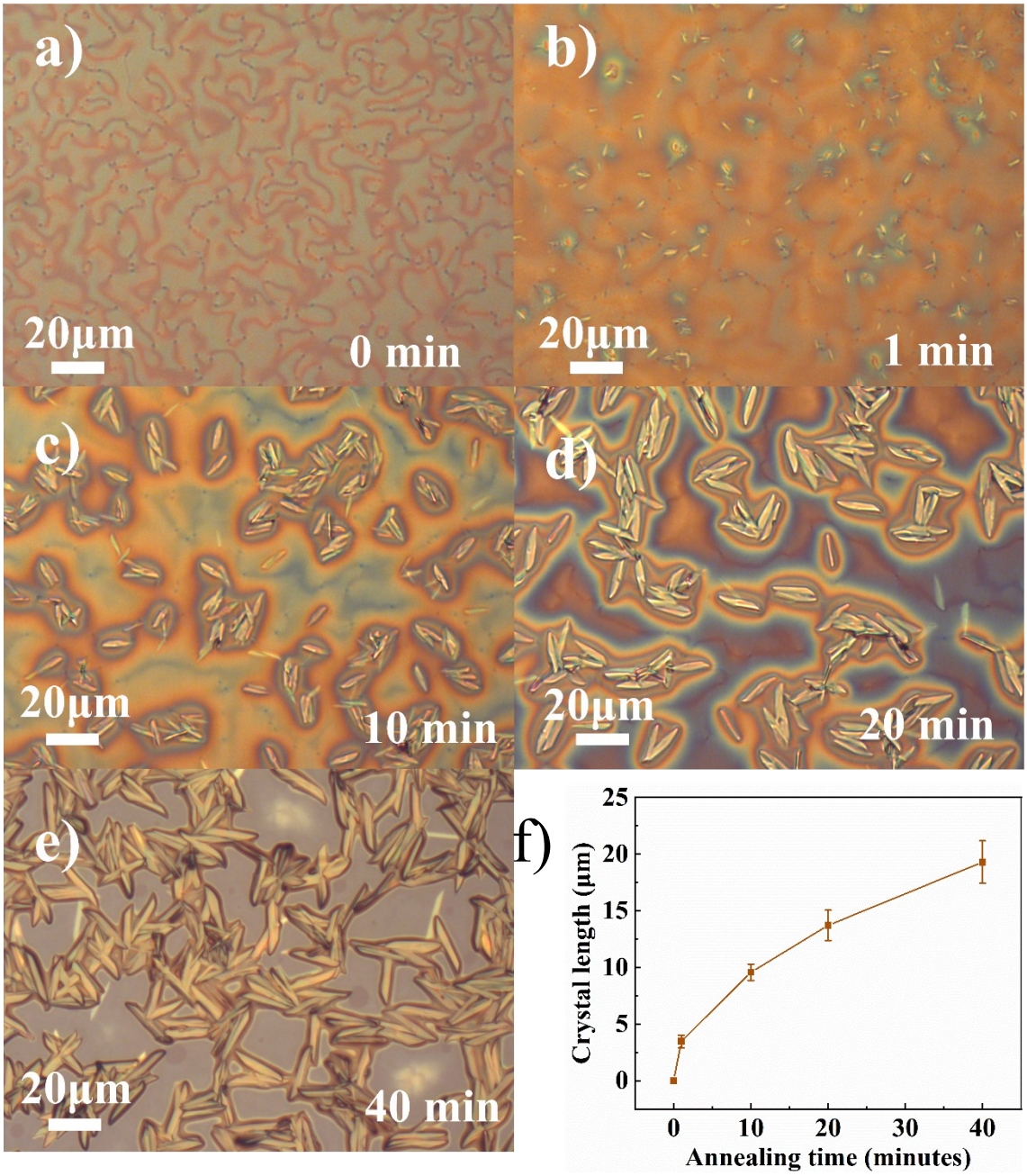

Fig. S13 Optical graphs of thin films that have undergone the 180°C annealing step, followed by rapid cooling and annealing at 145°C for various durations (a: no anneal, b: 1 min, c: 10 min, d: 20 min, e: 40 min). (f) Average size of the longer crystal axis as a function of annealing time. The crystal growth rate can be estimated to about 25 µm/h.

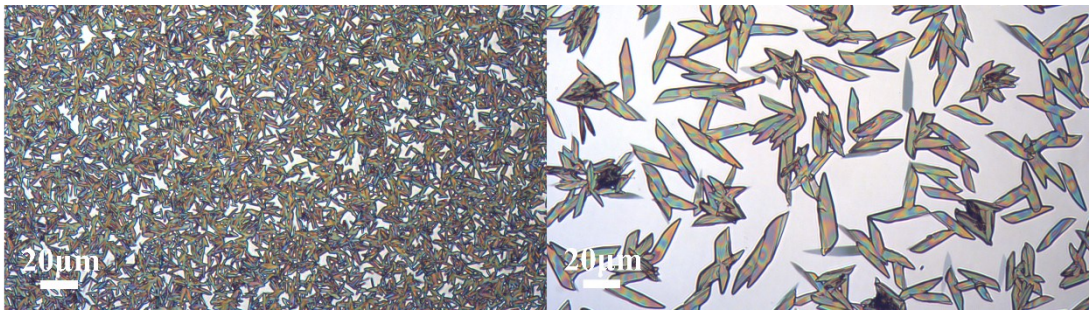

Fig. S14 Optical micrograph of a thin film after different annealing conditions. (a) 145 ℃ 40 minutes; (b) 180℃ 5 minutes followed by 145 ℃ 40 minutes. Substrate is silicon wafer.